Sugar-assisted Mechanochemical Exfoliation of Graphitic Carbon Nitride for Enhanced Visible-light Photocatalytic Performance

Wei Liu, Takashi Yanase, Nobuhiro Iwasa, Hitoshi Koizumi, Shin Mukai, Shinichiro Iwamura, Taro Nagahama, and Toshihiro Shimada*

Division of Applied Chemistry, Faculty of Engineering, Hokkaido University, Kita 13 Nishi 8, Kita-Ku, Sapporo, Hokkaido 060-8628, Japan.

*E-mail: shimadat@eng.hokudai.ac.jp

Abstract: A simple co-grinding treatment with fructose is introduced for the efficient and scalable preparation of g-C_3N_4 nanoplates. The results revealed that these g-C_3N_4 nanoplates still preserved the basic framework of carbon nitride and even displayed superior morphological properties and electronic structures. With respect to the pristine carbon nitride, the few-layered g-C_3N_4 impressively demonstrated an enhanced photocatalytic activity towards hydrogen generation and the degradation of Rhodamine B (RhB) under visible light illumination, emphasizing the vital roles of the morphology and electronic structures on the photocatalytic performance. This study provided sustainable and cost-effective tactics for the delamination of g-C_3N_4 for efficient energy conversion.

Key words: g-C_3N_4 nanoplates; co-grinding; sugar; photocatalytic activity

1. Introduction

Since the unveiling of the capability of the photosplitting of water for hydrogen evolution in 2009, polymeric carbon nitride has developed into a “hot” research area [1-5]. Although graphitic carbon nitride (g-C_3N_4) as a metal-free, versatile photocatalyst, exhibits environmental friendliness, low-cost and high chemical stability, it still requires sophisticated skills to suppress the unfavorable charge recombination as well as to increase the low surface area [6-12]. To date, there have been various attempts to adjust the features of g-C_3N_4 including the modification of its morphologies, the doping with heteroatoms, the modulation by copolymerization, and the creation of heterostructures [13-22]. Among these strategies, the formation of nano-sized morphologies is considered as a prospective method to improve its performance. The two-dimensional (2D) nanostructure endowed g-C_3N_4 nanoplates with distinctive features, such as high surface area, plentiful active sites and fast mobility of photogenerated charge carriers towards the in-plane direction, which provides them with a favorable prospect for photocatalysis [23-29].

Generally, 2D g-C_3N_4 nanoplates can be acquired by delamination of the bulk parent g-C_3N_4 through a range of methods, such as mechanical milling, thermal oxidation exfoliation, and liquid exfoliation [26,28,31-33]. Unfortunately, the liquid exfoliation strategies are normally involved in the use of organic solvents (IPA and DMF) and/or corrosive acids/alkalis [26,31-33], which are undesirable for sustainability. In addition, the thermal oxidation delamination process

also produces abundant hazardous gas upon decomposing of the carbon nitride framework [28]. Until now, only limited studies have been reported about the preparation of g-C_3N_4 nanoplates by the green delamination approaches such as sonication in pure water and the aqueous bithermal method [34-36]. The former sonication method suffers from the disadvantages of time consumption and the very low final concentration (less than 0.5 mg ml^{-1}), while the latter approach also requires abundant time and multiple processes to proceed.

Recently, mechanochemistry is of increasing interest for the fabrication and modification of the g-C_3N_4 nanoplates, which appears as an effective, green and economical strategy with respect to their liquid-phase counterparts [37-39]. For instance, Han et al. reported the iodine-assisted ball-milling method for the preparation of iodinated g-C_3N_4 nanoplates. The optimized sample showed an increased photocatalytic activity because of its high specific surface area, narrowed bandgap and well aligned band structure [38]. Furthermore, Ji et al. proposed the facile mechanical grinding approach for enhancing the electrochemiluminescent biosensing of pristine g-C_3N_4 with aromatic molecules. The g-C_3N_4 nanoplates are reported to be simultaneously exfoliated and modified by π-π stacking interactions [39]. It is noteworthy that the consumption of these detrimental and/or high-priced reagents limits the realization of scale-up and the ball-milling process also requires expensive laboratory equipment. Therefore, it remains a challenge to propose protocols for the delamination of g-C_3N_4 materials in a more sustainable, time-saving and cost-effective way.

Sugar crystals are readily available, recyclable and innocuous carbohydrates with abundant hydroxy groups. González et al. revealed that the sugars can function as an exfoliation agent

during the mechanochemical treatment of graphite and proved by a theoretical study [40]. Furthermore, solid sugar crystals have been recently used to exfoliate boron nitride, and dispersing boron nitride lamellae in water due to the covalent interactions [41]. Sugar interactions with inorganic layered nanomaterials were also explored by Chen and coworkers, who use natural sugars as green reactants to delaminate the transition-metal dichalcogenides (TMDs) by mechanical stirring [42].

Inspired by the above discussion on sugar-assisted mechanochemical treatment, we developed a simple and sustainable method for the efficient delamination of pristine g-C_3N_4 ~~nanoplates~~ via the co-grinding of pristine g-C_3N_4 in the presence of sugar. Thanks to the use of fructose, this co-grinding strategy led to the efficient delamination of the pristine g-C_3N_4 into few-layered g-C_3N_4 with a reasonable concentration of 2.3 mg mL^{-1}. With respect to the pristine g-C_3N_4, the water-soluble g-C_3N_4 nanoplates showed a high surface area, high exposure of active sites, relatively low surface defects, and fast transfer mobility of the photoinduced carriers. As expected, the as-obtained g-C_3N_4 nanoplates exhibited an impressively improved photocatalytic performance regarding the photosplitting of water for hydrogen evolution and the degradation of RhB.

2. Experimental details

2.1 Sample preparation

The pristine g-C_3N_4 was prepared by directly heating melamine up to 823 K for 4 h with a heating rate of 2.3 K min^{-1}. After the heat treatment, the resultant yellow agglomerates were cooled to ambient temperature, then ground into powder which was denoted as GCN.

The fructose-assisted synthesized few-layered g-C_3N_4 nanoplates were labeled as f-CNNP and prepared by the co-grinding of the bulk GCN and fructose in the following steps. Fructose and the as-prepared bulk GCN at the mass ratio of 1:5 were ground using a mortar and pestle for 2.5h at about 160 rpm. The milled powder was then dispersed in water at the initial concentration of 2 mg ml^{-1} and subjected to bath sonication for 1h. The mixture was centrifuged at 3000 rpm to remove the thick sheets. The supernatant was washed with 200 ml deionized water and filtered through a polytetrafluoroethylene (PTFE) membrane (pore size=0.47 μm). This procedure was repeated several times to thoroughly remove the excess fructose. The final samples after removing the water in a freeze-dryer were obtained with the yields of 37.5%. The samples prepared with sucrose instead of fructose were denoted as s-CNNP with the yields of 40%, respectively.

2.2 Photocatalyst characterization

The crystal structures were acquired using X-ray diffraction (XRD) technique on a Rigaku Miniflex 600. The Raman results were obtained on a Renishaw inVia reflex Raman microscope using a 785-nm excitation laser. The Fourier transform infrared (FTIR) spectra were performed on a JASCO FT/IR-4600. X-ray photoelectron spectroscopy (XPS) spectra were obtained using a JEOL JPS-9200. Scanning electron microscopy (SEM) images were obtained on a JEOL JEM-2010. Transmission electron microscopy (TEM) was conducted on a JEOL JEM-2010 TEM. The photoluminescence (PL) spectra were recorded on a JASCO FP-8000 excited at 365 nm. The diffuse reflectance spectra (DRS) were conducted on a UV-visible spectrometer (JASCO V-750). The Nitrogen adsorption and desorption isotherms were carried out on a Quantachrome

Autosorb-iQ2. The electron spin resonance (ESR) spectra were recorded on a JEOL JES-FA 200ESR (microwave power:100 μW, modulation frequency: 100 kHz). A gas chromatograph (GC-2014C, Shimadzu) is employed to measure the amount of the evolved H_2. Electrochemical impedance spectroscopy (EIS) were carried out on an electrochemical workstation (1260/1287, Solartron Analytical). The transient photocurrent response was recorded by using a Hokuto Denko HU-101 instrument with a traditional three-electrode cell. Typically, the ITO electrode deposited with the samples served as the working electrode, whereas a saturated Ag/AgCl electrode and a platinum sheet were the reference and counter electrodes, respectively. A 0.5 M Na_2SO_4 solution was employed as the electrolyte.

2.3 Photocatalytic Hydrogen Production Test

The Photocatalytic water splitting test was carried out in a glass container equipped with a silicone rubber stopper under visible light illumination. First, 30 mg photocatalyst was dispersed in a 10% triethanolamine aqueous solution. A 3 wt% Pt specimen as the co-catalyst was loaded via the *in situ* photo-deposition method using H_2PtCl_6 under 150-W xenon illumination for 1 h. The reaction solution was then bubbled with N_2 for 30 minutes to eliminate the air, followed by illumination using a 150 W xenon lamp with a 400 nm cut-off filter. The produced H_2 was tested using a gas chromatography within a thermal conductivity detector.

2.4 Photocatalytic RhB Degradation Test

The RhB removal test was carried out under visible light illumination. 25 mg of the photocatalyst was added in 50 mL of aqueous solution containing 10 mg/L of RhB. The dispersion was sonicated for 10 min, then stirred for 20 min in the dark to obtain the adsorption

equilibrium before the light irradiation. At 20-minute intervals, 3 mL of the solution was taken out and subjected to centrifugation to eliminate the photocatalyst. The concentration of Rhodamine B was estimated on a UV-visible spectrometer at 553 nm by analyzing the absorbance of the supernatant.

The reactive species in the RhB degradation process were analyzed by adding isopropanol (IPA), triethanolamine (TEOA) and benzoquinone (BQ) to the RhB dispersion as the scavengers for the hydroxyl radicals (•OH), superoxide holes (h+) and radicals ($\bullet O_2^-$), respectively.

3. Results and discussion

The main exfoliation process is illustrated in Fig. 1. A mixture of pristine g-C_3N_4 particles and sugar crystals were ground using a mortar and pestle during which both shearing and compressive forces existed between the g-C_3N_4 and sugar crystals. This leads to the production of small-sized and thinner g-C_3N_4. Simultaneously, the sugar crystals become attached to the continuously exposed surfaces of the g-C_3N_4, which could potentially result in the g-C_3N_4 reacting with the sugar molecules. Considering that g-C_3N_4 is a 2D nanomaterials analogous to graphite, it is assumed that the hydroxyl groups (–OH) in the structure of the sugars are associated with the interaction between the carbohydrates and g-C_3N_4 in a way similar to the delamination of the graphite during the mechanochemical treatment [40]. As a result, the f-CNNP obtained by a freeze-drying process could be homogeneously redispersed in water to form a stable suspension without obvious sediments up to 3 days (Fig. S1). For comparison, the pristine GCN was co-ground with NaCl under the same grinding conditions, which acted as an efficient medium for the disintegration of the nanodiamond aggregates [43]. However, no

obvious soluble g-C_3N_4 after grinding with NaCl (Fig. S2) was obtained. A similar phenomenon also appears when the pristine GCN was co-ground with melamine and boric acid under the identical conditions (Fig. S2). It is noted that raffinose crystals are also selected as the exfoliation agent under the same conditions with few-layered g-C_3N_4 dispersion concentration of 2mg ml^{-1}. These results reveal the important role of sugar in the exfoliation and modification of g-C_3N_4, which rendered the few-layered g-C_3N_4 easily dispersible in water.

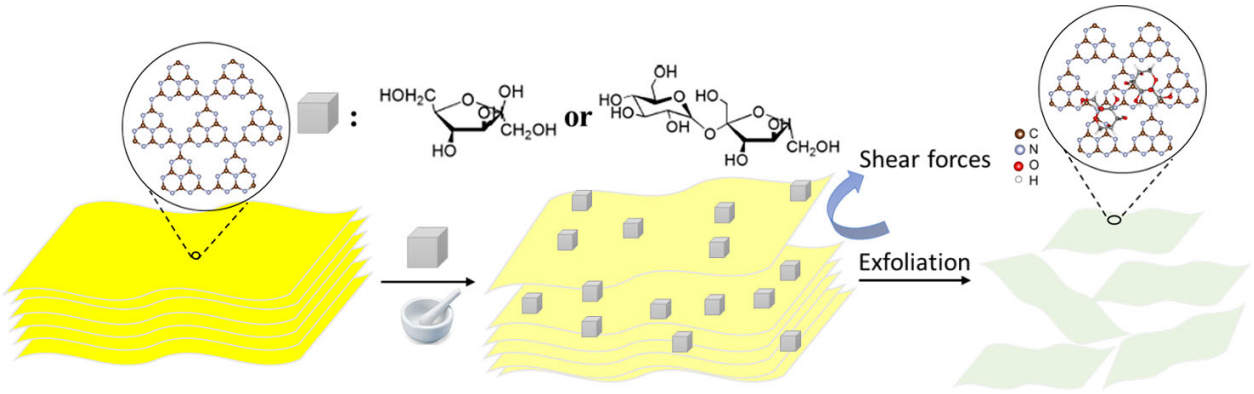

Fig.1 Illustration of the exfoliation procedure

The XRD patterns of the bulk GCN, f-CNNP and s-CNNP are compared in Fig. 2A. Two prominent diffraction peaks at around 27.4° and 13.1°, according to the (002) and (100) planes, can be observed in the XRD pattern of the pristine GCN sample and these two diffraction peaks are ascribed to the interlayer stacking of the conjugated aromatic g-C_3N_4 units and the in-plane stacking of the heptazine framework, respectively [44,45]. For the samples obtained by the sugar-assisted grinding, their diffraction peaks show positions similar to those of the pristine GCN sample, suggesting that the framework of the carbon nitride structure is retained during the grinding process, which is also evidenced by the Raman spectra of the samples. However, the exfoliated samples both show less pronounced peaks with respect to the pristine GCN sample,

indicating the high degree of reduction in the planar size and thickness of carbon nitride due to the effect of the milling-induced exfoliation [23,28]. The Raman spectra of the bulk GCN, f-CNNP and s-CNNP are shown in Fig. 2B in which the typical peaks of the heptazine structural backbone are identified by in the following description. The broad peak in the range of 1200–1700 cm^{-1} is due to the main C–N stretching vibrations. Two distinct peaks were observed at 708 and 978 cm^{-1}, which are associated with the breathing modes of the heptazine units [46,47]. It is noted that the Raman resonance of f-CNNP has a similar shape apart from the peak weakening with respect to that of the parent GCN, suggesting that the structure of f-CNNP is not altered during the milling process.

To detect the potential functional groups, the FTIR spectra of the pristine GCN and the sugar modified catalysts were investigated. Figure. 2C shows the FTIR spectra of the pristine GCN, f-CNNP and fructose, in which the spectra of the bulk GCN and f-CNNP showed similar absorption peaks. This indicates that the few-layered nanoplates maintained the typical chemical structure of the carbon nitride. The peaks between 1200 and 1650 cm^{-1} are interpreted as the stretching vibrations of the aromatic rings. The peaks around 811 cm^{-1} are associated with the tri-s-triazine rings and the broad peaks around 3300 cm^{-1} correspond to the stretching vibrational modes of the amine or hydroxyl groups [48-50]. Meanwhile, the absorption peaks for f-CNNP were blue-shifted to a higher wavenumber with respect to that of the bulk GCN, which was probably a result of the quantum confinement effect induced by the reduction of the particle size [37]. In particular, the additional peaks in the range of 2800~3000 cm^{-1} and 1073 cm^{-1} could be observed in the FTIR spectrum of f-CNNP (Fig. 2D), attributed to the C-H and C−O vibrations

of fructose, respectively [41]. The FTIR spectrum of s-CNNP is shown in Fig. S3, in which the C−OH stretching vibration of the sucrose also appeared.

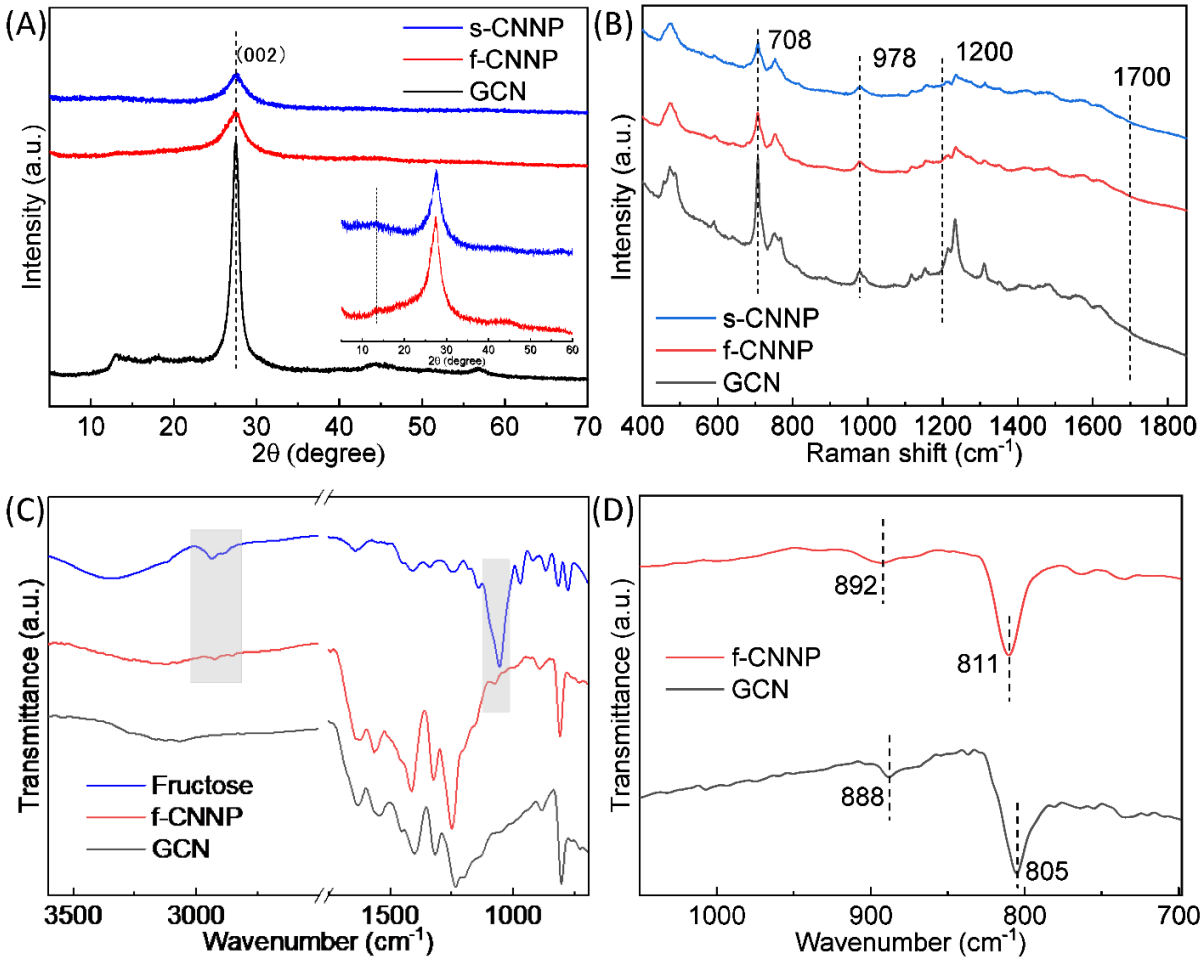

Fig. 2 (A) XRD patterns (B) Raman spectra, (C,D) FT-IR spectra of the as-prepared GCN and f-CNNP

XPS was performed to detect the composition and chemical states of the GCN and f-CNNP. Figure S4 shows the XPS survey spectrum for GCN, f-CNNP and s-CNNP with typical sharp peaks at binding energies of 285 eV (C 1s), 399 eV (N 1s) and 532 eV (O 1s). The appearance of the minor O signal probably due to the physically adsorbed oxygen. According to the

quantitative analysis from XPS, the C/N molar ratio of f-CNNP (0.78) slightly increased in comparison to that of GCN (0.76), suggesting the absorption of fructose on the surfaces for f-CNNP. The high resolution C1s XPS spectrum of the bulk GCN can be resolved into two typical peaks at 285.0 eV and 287.9 eV, which were assigned to the sp^2 C=C bonds and sp^2-hybridized bonds (C=N–C) in the heptazine rings, respectively, in Fig. 3A. Additionally, the C 1s XPS spectrum of f-CNNP can be separated into an additional peak at 286.1 eV apart from the above-mentioned two peaks, which is due to the sp^3 C ($C\text{-}(N)_3$) in the framework of carbon nitride [9,23,51]. It was noted that the peak of C=C for f-CNNP shifted to a lower binding energy compared to that of GCN, which suggests a minor change in the carbon atoms distribution. Figure. 3B descripts the high resolution N1s spectrum of f-CNNP, which is very similar to that of the bulk GCN. Four typical peaks located at about 398.4 eV, 399.4 eV, 400.8 eV, and 404.2 eV can be obtained after the deconvolution of the N 1s spectra and originate from the sp^2-hybridized C=N–C, $N–(C)_3$, N–H and π excitation, respectively [9,23,52]. The f-CNNP had the same nitrogen species as those of the pristine GCN, and the peak area percentage of the C–N=C to $N–(C)_3$ experienced a moderate increase from 2.83 (GCN) to 3.30 (f-CNNP) (Table S1) based on XPS analyses. The decreased ratio of $N–(C)_3$ for the f-CNNP possibly resulted from the fracture of sp^3 $N–(C)_3$ bonds induced by the grinding exfoliation. In general, these results above revealed a small change in the chemical states of f-CNNP after the co-grinding process in the presence of fructose and suggested the absorption of sugar molecules on the surface of the f-CNNP. The XPS of s-CNNP was also performed, which is presented in Fig. S5.

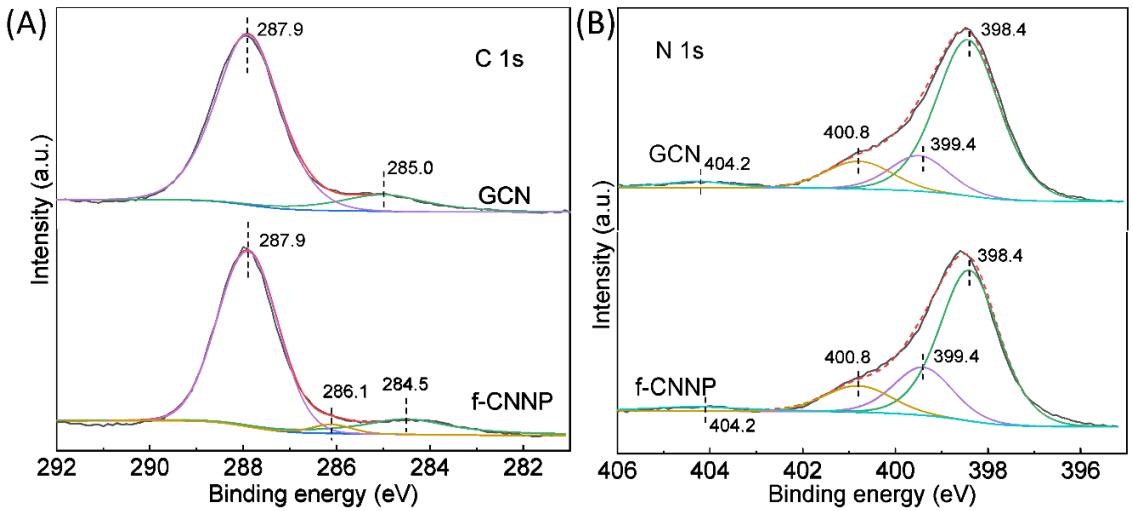

Fig. 3 High-resolution (A) C1s and (B) N1s XPS spectra of the as-synthesized (a) GCN and (b)f-CNNP

The morphologies of the bulk GCN, f-CNNP and s-CNNP were investigated by SEM and TEM. The pristine bulk GCN shows thick and aggregated layers with a large lateral size (~3 μm) and thickness (~100 nm) (Fig. S6). However, with the assistance of the fructose crystals, the f-CNNP sample was ruptured and exfoliated and showed the aggregate size of ~200 nm and thickness <5 nm after the 2.5 h milling (Fig. 4A). The lateral size s-CNNP sample even became less (~100 nm) after the 2.5 h milling in the presence of the sucrose crystals (Fig. 4B). TEM images also revealed that the as-obtained f-CNNP and s-CNNP with a laminar morphology are almost transparent, indicating their ultrathin thickness (Fig. 4C) [53]. AFM measurements further confirmed that the average thickness of the f-CNNP was around 3 nm (Figure S7). For a fair comparison, the sonication of the bulk GCN in the aqueous fructose solution was explored. The resulting suspension after centrifugation appears clear and transparent in contrast to the milky

f-CNNP dispersion prepared in the presence of fructose (Figure S8A). This result suggests that the density of the CNNP was very low showing the important effect of grinding on the exfoliation of the CNNP. Furthermore, the manual grinding of bulk GCN without fructose followed by sonication was also conducted. As a result, the suspension after centrifugation also looks transparent (Figure S8B). The result reflects the fact that the addition of fructose crystal makes a difference in the effective exfoliation and modification of carbon nitride during the grinding process.

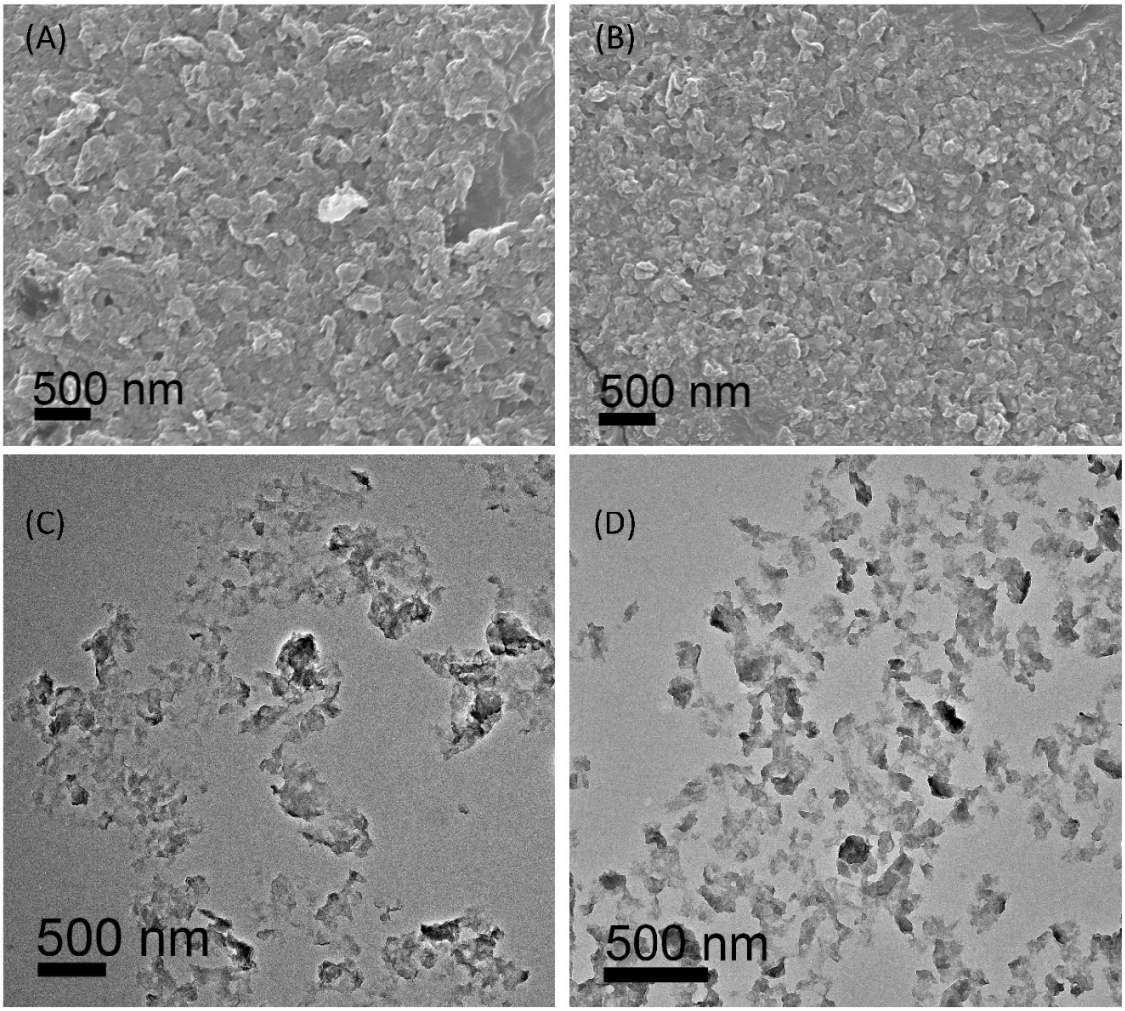

Fig. 4 Typical SEM of the as-synthesized (A) f-CNNP and (B) s-CNNP. TEM images of as-synthesized (C) f-CNNP and (D) s-CNNP.

As shown in Fig. 5, the nitrogen adsorption-desorption isotherms of the bulk GCN, f-CNNP and s-CNNP revealed that all of the samples exhibited type *IV* adsorption-desorption isotherms with a high adsorption capacity in the relative pressure range of 0.8–1.0, which suggests the presence of abundant mesopores and macropores [54-56]. The specific surface area of the f-CNNP and s-CNNP were 57.4 m^2 g^{-1} and 81.3 m^2 g^{-1}, which is about 6 and 8 times the value of the bulk GCN (10.1 m^2 g^{-1}), respectively. The Barret–Joyner–Halenda (BJH) results reveal that f-CNNP has a wide pore size distribution between 10 and 200 nm. Additionally, incremental average pore volumes of f-CNNP and s-CNNP (0.2676 cm^3 g^{-1} for f-CNNP and 0.3020 cm^3 g^{-1} for s-CNNP) were confirmed with respect to that of the bulk GCN (0.064 cm^3 g^{-1}). These pores probably originate from the slit-like pores present among the stacked nanoplates. The increased surface area and few-layered structure of the photocatalysts are beneficial to the generation of more reactive sites for adsorbing more reactants as well as the prompt charge transfer to the surface active sites, which favor the photocatalysis.

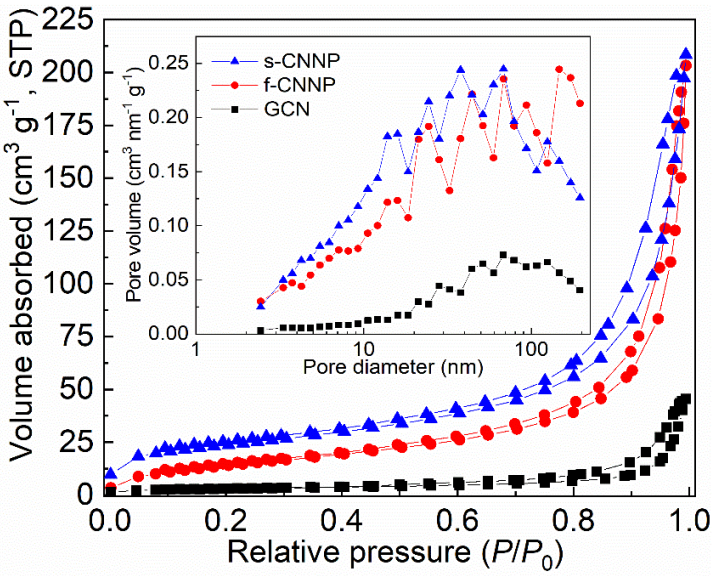

Fig. 5 N_2 adsorption/desorption isotherms of the as-synthesized GCN, f-CNNP and s-CNNP. The inset is the corresponding pore size distribution plots

The optical properties of the samples were explored by the UV-vis diffuse reflectance and photoluminescence (PL) spectra. As displayed in Fig. 6A, the absorption band of the three samples have similar UV-vis spectra shapes except for a blue shift of the absorption edge from 480 nm for the bulk GCN to 450 nm for f-CNNP and s-CNNP. The corresponding bandgaps for the bulk GCN, f-CNNP and s-CNNP were calculated to be 2.75, 3.0 and 3.0 eV, respectively, by deducing the linear region of the Tauc plots. The increased bandgap of f-CNNP results from the decreased particle size and thickness, which is related to the quantum confinement effect [56,57]. This effect is also evidenced by the PL spectra (Fig. 6B), where the emission peak of the bulk GCN experienced a blue-shift from 474 nm to 455 nm for the f-CNNP. The broad PL emission peak is associated with the radiative recombination of the photoinduced charge carriers [58]. This phenomenon well agrees with the absorption edge extension toward the long wavelength

according to the UV-Vis absorption results. To further determine the existence of unpaired electrons in the photocatalysts, ESR spectroscopy was performed on the samples. As shown in Fig. 6C, the samples display one single Lorentzian line with a g value of 2.0035, which is induced by the unpaired electrons in the conduction band of carbon nitride [59]. With respect to the pristine GCN, an obvious stronger signal for the unpaired electrons of f-CNNP and s-CNNP can be observed, which facilitated the photogeneration of the active radical pairs for the photocatalytic reactions [52].

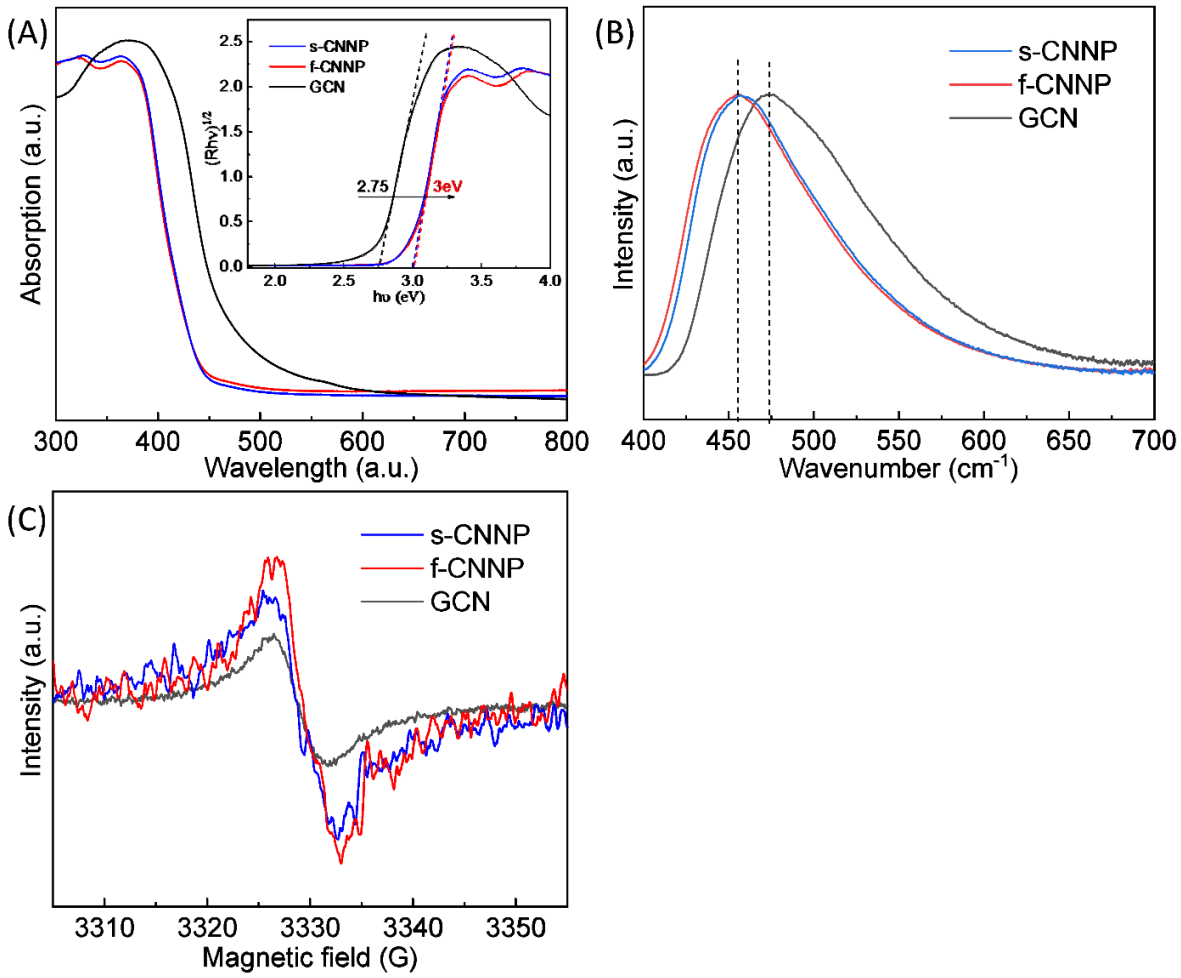

Fig. 6 (A) UV-vis absorption spectra, (B) PL emission spectra and (C) ESR spectra of the as-synthesized GCN, f-CNNP and s-CNNP

The transient photocurrent of the bulk GCN, f-CNNP and s-CNNP electrodes were measured for several one-off irradiation cycles, as shown in Fig. 7A. It is known that the photocurrent measurement indirectly reflects the recombination rate of the carriers and the higher photocurrent density represents the higher ability of the sample to generate and transfer photogenerated charge carriers. For each illumination, a rapid photocurrent signal was recorded in these samples and deduced that the photocurrent is replicable. The f-CNNP and s-CNNP exhibited similar photocurrent densities but higher than the parent GCN under illumination, indicating that the exfoliation has rendered the samples suppressed electron-hole recombination and promoted charge carrier separation. EIS was further conducted to evaluate the interfacial charge transfer of the three samples. As displayed in Fig. 7B, the semicircle arc radius of the samples showed the size growth of f-CNNP < s-CNNP < GCN, which indicates the lower charge transfer resistance thus faster charge mobility in CNNP because of their ultrathin structures.

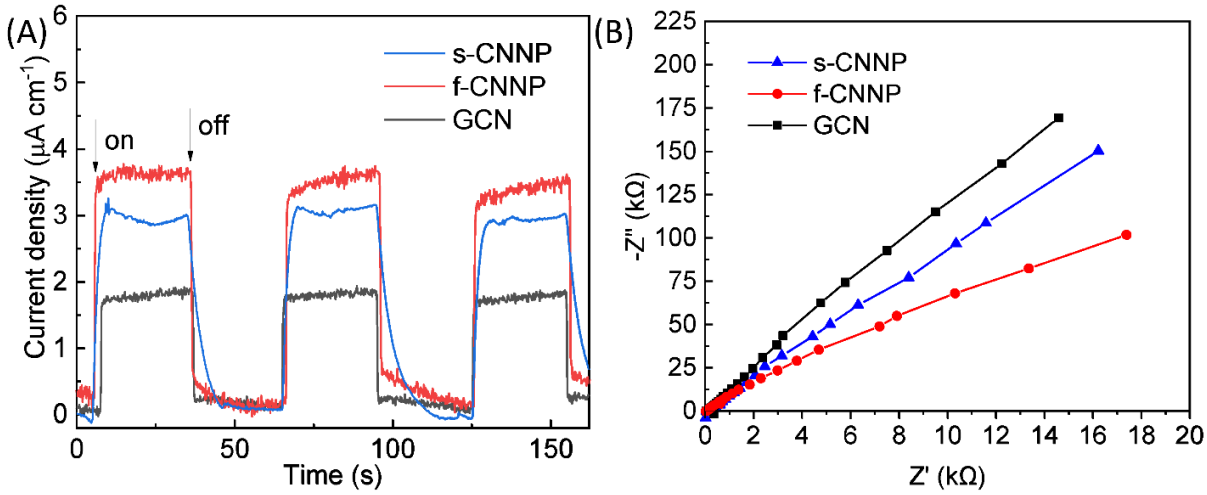

Fig. 7 (A) transient photocurrent results and (B) Nyquist plots of EIS of the as-synthesized GCN, f-CNNP and s-CNNP

To further investigate the influence of exfoliation on the valence band maximum (VBM) and conduction band minimum (CBM) of the samples, valence-band X-ray photoelectron spectroscopy (XPS) was carried out (Fig. 8A). The XPS valence band results show that the VBM of the bulk GCN, f-CNNP and s-CNNP were estimated to be 1.99, 1.94 and 1.99 eV, respectively. Combined with the bandgap energies derived from Fig. 5b, the CBM of the bulk GCN, f-CNNP and s-CNNP were calculated to be -0.76, -1.06 and -1.01 eV, respectively, indicating a negative shift of about 0.3 and 0.25 eV for f-CNNP and s-CNNP, respectively. Based on the VB potential and band gap, the electronic band structures of the bulk GCN, f-CNNP and s-CNNP catalysts are illustrated in Fig. 8B. With respect to the pristine GCN, the CB of f-CNNP and s-CNNP were upshifted, which demonstrated a stronger reducibility during the photocatalytic reactions [57,60].

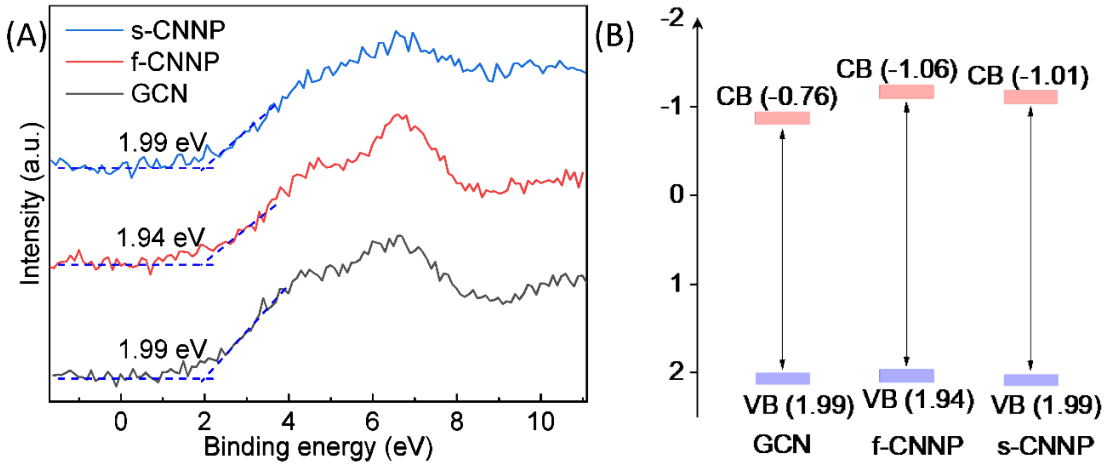

Fig. 8 (A) XPS valence band spectra and (B) electronic band structures of the as-synthesized GCN, f-CNNP and s-CNNP

The photosplitting of water for hydrogen evolution of the bulk GCN, f-CNNP and s-CNNP was tested under visible light illumination (>400 nm). Figure 9A shows the H_2 evolution rate of the samples under visible light irradiation. The bulk GCN displays a small photocatalytic H_2 production rate of 37.7 μmol h^{-1} g^{-1}, whereas the rate of H_2 evolution reached 103.7 μmol h^{-1} g^{-1} and 66.7 μmol h^{-1} g^{-1} for f-CNNP and s-CNNP, respectively. The H_2-evolution rate of s-CNNP outperforms that of bulk GCN by nearly two-fold, and f-CNNP could also enhance the hydrogen production about three-fold, proving that delaminating it into few-layered g-C_3N_4 is favorable for improving the photocatalytic H_2 production of the g-C_3N_4-based materials. Moreover, f-CNNP also shows a sustainable photocatalytic H_2 evolution without obvious reduction after three cycles up to 12 hours, validating its high stability (Fig. 9B). The XRD pattern of the f-CNNP after three cycles of photocatalytic H_2 production was also collected, which further verified its impressive stability (Fig. S9). When it is illuminated by the full spectrum of the Xe lamp, FA-fl-CN

demonstrates a promoted hydrogen evolution rate of 690 μmol h^{-1} g^{-1}, higher than the other two samples (309 μmol h^{-1} g^{-1} for SA-fl-CN and for 181 μmol h^{-1} g^{-1} for GCN) (Fig. 9C). The effect of variations in weight ratio (1:3, 1:4, 1:5, 1:6 and 1:7) of GCN:fructose on the photocatalytic performance were also explored with a mechanochemical treatment time of 2.5 h, as displayed in Fig. S10. In this study, the weight ratio of GCN:fructose was fixed at 1:5 to obtain f-CNNP with suitable hydrogen production rate at low cost. The significantly enhanced photocatalytic performance of the f-CNNP towards water splitting can be possibly understood by several reasons. First, a better dispersibility of f-CNNP in the reaction solution and the generation of more active sites due to the increased specific surface area have a synergistic effect on the full contact of the catalytic species with the carbon nitride materials. Furthermore, the contribution from quantum confinement, which is induced by the reduced size and thickness of f-CNNP, speeds up the migration and separation of the photogenerated carriers [61]. It is noteworthy that the surface area probably is not very critical in the water splitting activities as in the photodegradation of organic pollutants, because for uphill reaction of water splitting, the crystallinity becomes the more dominant factor [62].

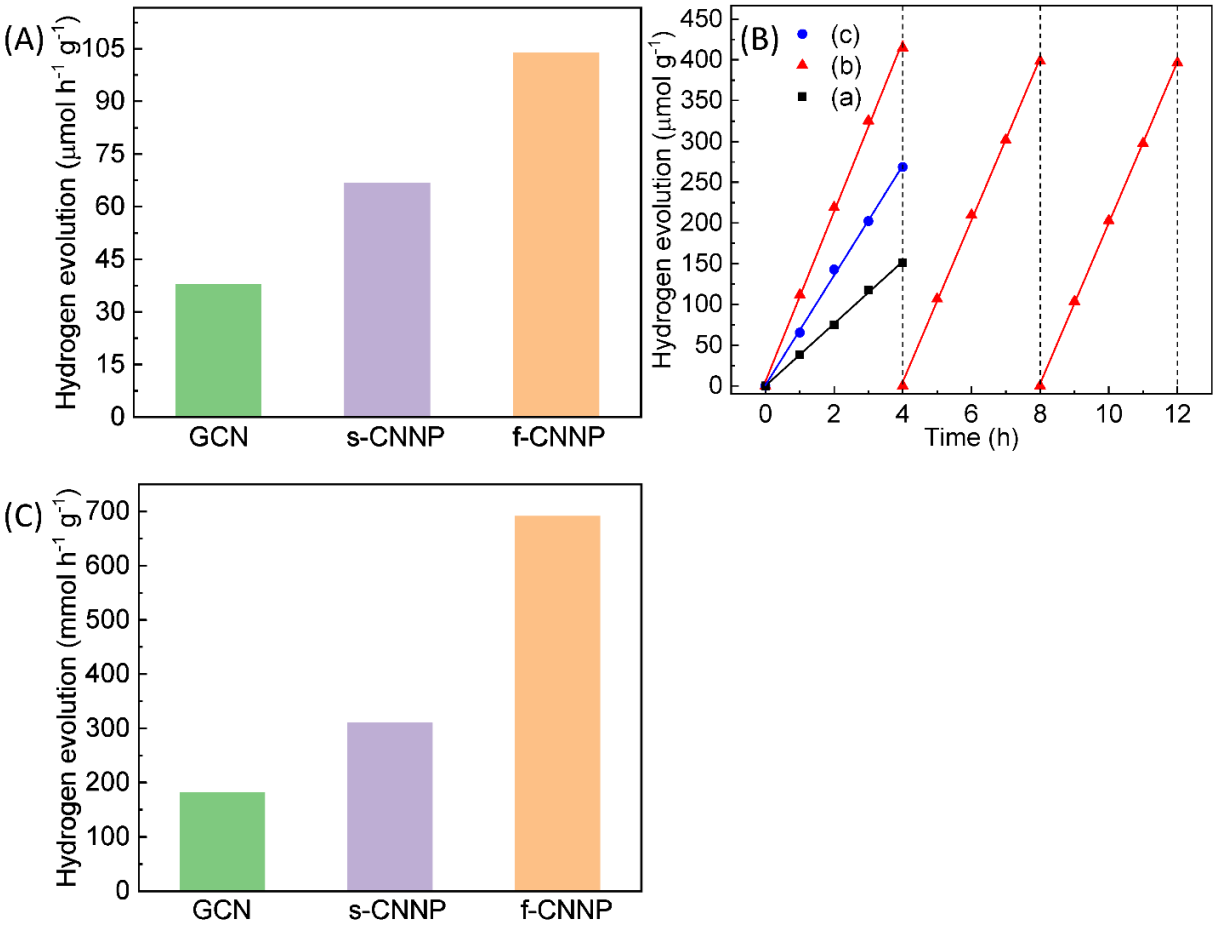

Fig. 9 (A) Visible-light hydrogen evolution rate, (B) stability test of hydrogen production and (C) hydrogen production rate under full spectrum illumination over the as-synthesized (a) GCN, (b) f-CNNP and (c) s-CNNP.

The photocatalytic performance of the samples were further tested by the degradation of RhB under visible light illumination ($\lambda > 400$ nm), as shown in Fig. 10A. As expected, the f-CNNP and s-CNNP samples show superior degradation rates vs. that of GCN. f-CNNP outperformed the other two samples with an excellent photocatalytic performance and could remove about 98% of RhB within 120 min exposed under irradiation, while only 17% of RhB was decomposed in the presence of GCN under the same reaction conditions. The stability of the photodegradation of

RhB for four cycles under the identical conditions revealed the good photocatalytic stability of the f-CNNP (Fig. S11). The kinetic behaviors for the RhB degradation of the catalysts were further investigated by fitting the experimental data using the pseudo-first-order correlation. The plots for the calculation of the apparent reaction constants (k) are shown in Fig. 10B. Correspondingly, it was noted that the f-CNNP exhibited the best photodegradation performance and the k value for the RhB degradation reached 0.0182 min^{-1} for f-CNNP and 0.0171 min^{-1} for s-CNNP, over 16 times higher than that of the GCN sample (0.00113 min^{-1}).

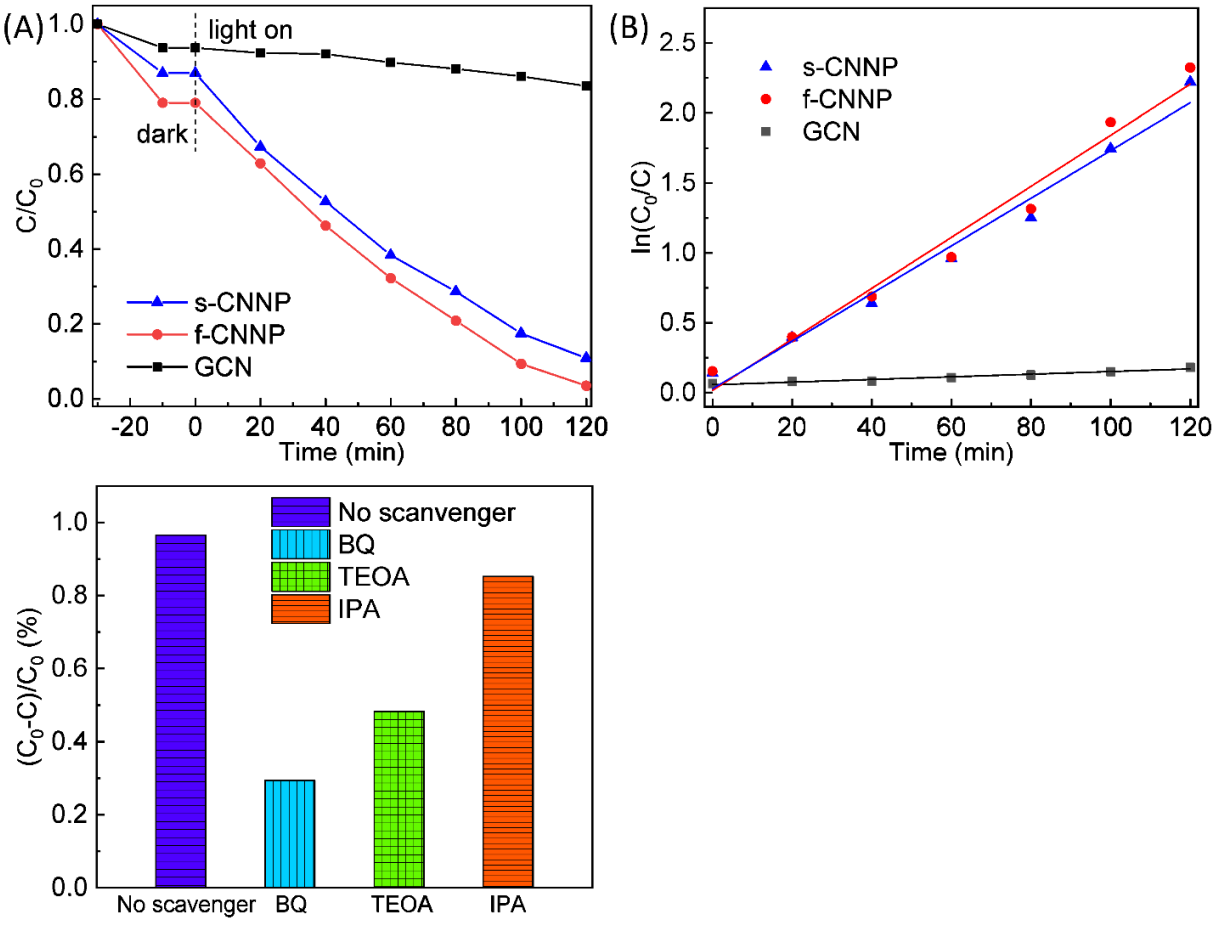

Fig. 10 (A) Photocatalytic oxidation of RhB for GCN, f-CNNP and s-CNNP and (B) the

corresponding apparent reaction constants (*k*) calculation plots under the visible light irradiation. (C) The effect of reactive species on the photocatalytic degradation of RhB solution by f-CNNP.

The active species trapping experiments for f-CNNP were performed to explore the photocatalytic mechanism of the RhB degradation. Isopropanol (IPA), triethanolamine (TEOA) and benzoquinone (BQ) were used as scavengers for the hydroxyl radical (•OH), photogenerated holes (h+) and superoxide radical ($\bullet O_2^-$), respectively [63,64]. As a result, after adding BQ to the reaction solution, the photodegradation efficiency was remarkably retarded, revealing that the $\bullet O_2^-$ served as the main active species for the degradation process (Fig. 10C). When TEOA was added, the photodegradation efficiency of RhB was moderately decelerated, suggesting the h+ is also responsible for the photodegradation reaction. When the IPA was dropped in reaction system, the photodegradation efficiency showed a slight decrease, suggesting that the •OH makes a smaller contribution to the RhB degradation than the $\bullet O_2^-$ and h+ radicals. Therefore, the $\bullet O_2^-$ and h+ radicals belong to the major reactive species in the f-CNNP reaction system.

As displayed in Fig. 11, the photocatalyst is irradiated upon the absorption of visible light and the e^-/h^+ pairs can be generated in CB and VB. It was noticed that the CB potential of f-CNNP (−1.06 eV vs NHE) is more negative than the potential of $O_2/\bullet O_2^-$(−0.33 V vs NHE) and thus capable to reduce the dissolved oxygen to form $\bullet O_2^-$ [65]. Oxygen molecules can also react with e^- and H^+ to generate H_2O_2 ($E^0(O_2/H_2O_2)$ = +0.695 eV). Afterwards, H_2O_2 molecules harvest electrons to produce •OH radicals ($O_2 + e^- \rightarrow \bullet O_2^-$, $\bullet O_2^- + e^- + 2H^+ \rightarrow H_2O_2$, $H_2O_2 + e^- \rightarrow \bullet OH + OH^-$). However, the holes in the VB potential of f-CNNP (+1.94 eV vs NHE) can't

effectively produce •OH radicals through oxidation of OH^- ($E^0(OH^-/•OH)$ =+1.90 eV vs NHE) [65]. Accordingly, the photoinduced holes are capable to directly degrade the adsorbed RhB molecules. During the hydrogen evolution, the sacrificial reagents are oxidized by holes. The excited electrons moved to cocatalyst Pt and reacted with H^+ to form H_2. The 2D structure of f-CNNP can offer more reactive sites to accommodate the reactants on the surface. Moreover, the increased bandgap also favors the generation of more photoexcited electrons. Therefore, the 2D structure is conductive to the improvement of the photocatalytic activity.

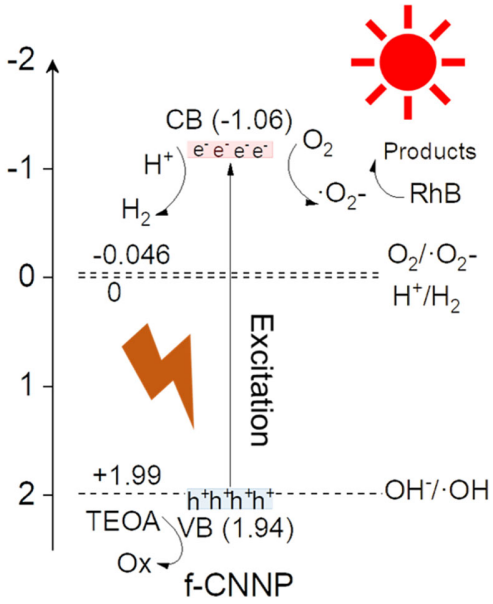

Fig. 11 The mechanism for photocatalytic activity over f-CNNP photocatalyst.

4. Conclusion

In summary, solid-state mechanical milling with sugars was successfully developed to exfoliate graphitic carbon nitride in a simple, sustainable and efficient way. The few-layered g-C_3N_4 products still maintained the framework of the carbon nitride and the original photoelectrical properties were basically preserved. With respect to the pristine GCN, the

sugar-assisted exfoliated few-layered g-C_3N_4 samples demonstrated an enhanced photocatalytic H_2 generation and degradation efficiency of RhB under the visible-light illumination due to the synergistic effects of the improved dispersion property induced by the reduced thickness and particle size, the enlarged specific surface area and fast mobility of the charge carriers along the in-plane direction. It is anticipated that our work can offer inspirations for the preparation of g-C_3N_4 nanoplates with a promoted visible light responsivity for the photocatalytic applications.

Acknowledgements

The authors are grateful to Professors H. Habazaki, C. Y. Zhu, M. Higuchi, Y. Masubuchi, K. Tadanaga, A. Miura, C. Rosero-Navaro and Ms. Ning Wang for their valuable discussions and experimental facilities. The present research was partly supported by KAKENHI (17H03380) from MEXT, Japan. The instrumental analyses were supported by the Nanotechnology Platform at Hokkaido University by METI, Japan. W.L. thanks the fellowship from the China Scholarship Council (201706950010).

Appendix A. Supporting information

Figures S1−S9, Table S1

Notes

The authors declare no competing financial interest.

References

[1] Wang X, Maeda K, Thomas A, Takanabe K, Xin G, Carlsson JM, et al. A metal-free polymeric photocatalyst for hydrogen production from water under visible light. Nat Mater 2009;8:76.

[2] Shekofteh-Gohari M, Habibi-Yangjeh A, Abitorabi M, Rouhi A. Magnetically separable nanocomposites based on ZnO and their applications in photocatalytic processes: a review. Crit Rev Environ Sci Technol 2018;48:806-57.

[3] Pirhashemi M, Habibi-Yangjeh A, Pouran SR. Review on the criteria anticipated for the fabrication of highly efficient ZnO-based visible-light-driven photocatalysts. J Ind Eng Chem 2018;62:1-25.

[4] Akhundi A, Habibi-Yangjeh A, Abitorabi M, Rahim Pouran S. Review on photocatalytic conversion of carbon dioxide to value-added compounds and renewable fuels by graphitic carbon nitride-based photocatalysts. Catal Rev 2019;61:595-628.

[5] Mousavi M, Habibi-Yangjeh A, Pouran SR. Review on magnetically separable graphitic carbon nitride-based nanocomposites as promising visible-light-driven photocatalysts. J Mater Sci: Mater Electron 2018;29:1719-47.

[6] Thomas A, Fischer A, Goettmann F, Antonietti M, Müller J-O, Schlögl R, et al. Graphitic carbon nitride materials: variation of structure and morphology and their use as metal-free catalysts. J Mater Chem 2008;18:4893-908.

[7] Cao S, Low J, Yu J, Jaroniec M. Polymeric photocatalysts based on graphitic carbon nitride. Adv Mater 2015;27:2150-76.

[8] Ong W-J, Tan L-L, Ng YH, Yong S-T, Chai S-P. Graphitic carbon nitride (g-C_3N_4)-based photocatalysts for artificial photosynthesis and environmental remediation: are we a step closer to achieving sustainability? Chem Rev 2016;116:7159-329.

[9] Liang Q, Li Z, Huang ZH, Kang F, Yang QH. Holey graphitic carbon nitride nanosheets

with carbon vacancies for highly improved photocatalytic hydrogen production. Adv Funct Mater 2015;25:6885-92.

[10] Zhang J, Chen Y, Wang X. Two-dimensional covalent carbon nitride nanosheets: synthesis, functionalization, and applications. Energy Environ Sci 2015;8:3092-108.

[11] Hong Y, Li C, Li D, Fang Z, Luo B, Yan X, et al. Precisely tunable thickness of graphitic carbon nitride nanosheets for visible-light-driven photocatalytic hydrogen evolution. Nanoscale. 2017;9:14103-10.

[12] Patnaik S, Martha S, Acharya S, Parida K. An overview of the modification of g-C_3N_4 with high carbon containing materials for photocatalytic applications. Inorg Chem Front 2016;3:336-47.

[13] Chang C, Zhu L, Wang S, Chu X, Yue L. Novel mesoporous graphite carbon nitride/BiOI heterojunction for enhancing photocatalytic performance under visible-light irradiation. ACS Appl Mater Interfaces 2014;6:5083-93.

[14] Lin Z, Wang X. Nanostructure engineering and doping of conjugated carbon nitride semiconductors for hydrogen photosynthesis. Angew Chem 2013;125:1779-82.

[15] Niu P, Yin LC, Yang YQ, Liu G, Cheng HM. Increasing the visible light absorption of graphitic carbon nitride (Melon) photocatalysts by homogeneous self-modification with nitrogen vacancies. Adv Mater 2014;26:8046-52.

[16] Liang Q, Li Z, Yu X, Huang ZH, Kang F, Yang QH. Macroscopic 3D porous graphitic carbon nitride monolith for enhanced photocatalytic hydrogen evolution. Adv Mate 2015;27:4634-9.

[17] Liu J, Huang J, Zhou H, Antonietti M. Uniform graphitic carbon nitride nanorod for efficient photocatalytic hydrogen evolution and sustained photoenzymatic catalysis. ACS Appl Mater Interfaces 2014;6:8434-40.

[18] Nayak S, Mohapatra L, Parida K. Visible light-driven novel g-C_3N_4/NiFe-LDH composite photocatalyst with enhanced photocatalytic activity towards water oxidation and reduction reaction. J Mater Chem A 2015;3:18622-35.

[19] Habibi-Yangjeh A, Mousavi M. Deposition of $CuWO_4$ nanoparticles over g-C_3N_4/Fe_3O_4 nanocomposite: Novel magnetic photocatalysts with drastically enhanced performance under visible-light. Adv Powder Technol 2018;29:1379-92.

[20] Mousavi M, Habibi-Yangjeh A. Magnetically recoverable highly efficient visible-light-active g-C_3N4/Fe_3O_4/Ag_2WO_4/AgBr nanocomposites for photocatalytic degradations of environmental pollutants. Adv Powder Technol 2018;29:94-105.

[21] Asadzadeh-Khaneghah S, Habibi-Yangjeh A, Seifzadeh D. Graphitic carbon nitride nanosheets coupled with carbon dots and BiOI nanoparticles: boosting visible-light-driven photocatalytic activity. J Taiwan Inst Chem Eng 2018;87:98-111.

[22] Habibi-Yangjeh A, Mousavi M, Nakata K. Boosting visible-light photocatalytic performance of g-C_3N_4/Fe_3O_4 anchored with $CoMoO_4$ nanoparticles: novel magnetically recoverable photocatalysts. J Photochem Photobiol A 2019;368:120-36.

[23] Yang S, Gong Y, Zhang J, Zhan L, Ma L, Fang Z, et al. Exfoliated graphitic carbon nitride nanosheets as efficient catalysts for hydrogen evolution under visible light. Adv Mater 2013;25:2452-6.

[24] She X, Xu H, Xu Y, Yan J, Xia J, Xu L, et al. Exfoliated graphene-like carbon nitride in organic solvents: enhanced photocatalytic activity and highly selective and sensitive sensor for the detection of trace amounts of Cu^{2+}. J Mater Chem A 2014;2:2563-70.

[25] Liu W, Iwasa N, Fujita S, Koizumi H, Yamaguchi M, Shimada T. Porous graphitic carbon nitride nanoplates obtained by a combined exfoliation strategy for enhanced visible light photocatalytic activity. Appl Surf Sci 2020;499:143901.

[26] Lin Q, Li L, Liang S, Liu M, Bi J, Wu L. Efficient synthesis of monolayer carbon nitride 2D nanosheet with tunable concentration and enhanced visible-light photocatalytic activities. Appl Catal B-environ 2015;163:135-42.

[27] Xu J, Zhang L, Shi R, Zhu Y. Chemical exfoliation of graphitic carbon nitride for efficient heterogeneous photocatalysis. J Mater Chem A 2013;1:14766-72.

[28] Niu P, Zhang L, Liu G, Cheng HM. Graphene-like carbon nitride nanosheets for improved photocatalytic activities. Adv Funct Mater 2012;22:4763-70.

[29] Xu H, Yan J, She X, Xu L, Xia J, Xu Y, et al. Graphene-analogue carbon nitride: novel exfoliation synthesis and its application in photocatalysis and photoelectrochemical selective detection of trace amount of Cu^{2+}. Nanoscale. 2014;6:1406-15.

[30] Bojdys MJ, Severin N, Rabe JP, Cooper AI, Thomas A, Antonietti M. Exfoliation of crystalline 2D carbon nitride: thin sheets, scrolls and bundles via mechanical and chemical routes. Macromol Rapid Commun 2013;34:850-4.

[31] Sano T, Tsutsui S, Koike K, Hirakawa T, Teramoto Y, Negishi N, et al. Activation of graphitic carbon nitride (g-C_3N_4) by alkaline hydrothermal treatment for photocatalytic NO

oxidation in gas phase. J Mater Chem A 2013;1:6489-96.

[32] Zhao F, Cheng H, Hu Y, Song L, Zhang Z, Jiang L, et al. Functionalized graphitic carbon nitride for metal-free, flexible and rewritable nonvolatile memory device via direct laser-writing. Sci Rep 2014;4:5882.

[33] Du X, Zou G, Wang Z, Wang X. A scalable chemical route to soluble acidified graphitic carbon nitride: an ideal precursor for isolated ultrathin g-C_3N_4 nanosheets. Nanoscale 2015;7:8701-6.

[34] Zhang X, Xie X, Wang H, Zhang J, Pan B, Xie Y. Enhanced photoresponsive ultrathin graphitic-phase C_3N_4 nanosheets for bioimaging. J Am Chem Soc 2012;135:18-21.

[35] Pattnaik SP, Behera A, Acharya R, Parida K. Green exfoliation of graphitic carbon nitride towards decolourization of Congo-Red under solar irradiation. J Environ Chem Eng 2019;7:103456.

[36] Pattnaik SP, Behera A, Martha S, Acharya R, Parida K. Facile synthesis of exfoliated graphitic carbon nitride for photocatalytic degradation of ciprofloxacin under solar irradiation. J Mater Sci 2019;54:5726-42.

[37] Kim JS, Oh JW, Woo SI. Investigation for the effects of ball milling process on the physical characteristics, the behaviors of carriers and the photocatalytic activity of sulfur doped g-C_3N_4. Int J Hydrogen Energy 2017;42:5485-95.

[38] Han Q, Hu C, Zhao F, Zhang Z, Chen N, Qu L. One-step preparation of iodine-doped graphitic carbon nitride nanosheets as efficient photocatalysts for visible light water splitting. J Mater Chem A 2015;3:4612-9.

[39] Ji J, Wen J, Shen Y, Lv Y, Chen Y, Liu S, et al. Simultaneous noncovalent modification and exfoliation of 2D carbon nitride for enhanced electrochemiluminescent biosensing. J Am Chem Soc 2017;139:11698-701.

[40] González VJ, Rodríguez AM, León V, Frontiñán-Rubio J, Fierro JLG, Durán-Prado M, et al. Sweet graphene: exfoliation of graphite and preparation of glucose-graphene cocrystals through mechanochemical treatments. Green chem 2018;20:3581-92.

[41] Chen S, Xu R, Liu J, Zou X, Qiu L, Kang F, et al. Simultaneous Production and Functionalization of Boron Nitride Nanosheets by Sugar-Assisted Mechanochemical Exfoliation. Adv Mater 2019;31:1804810.

[42] Chen K, Zhang W, Pan X, Huang L, Wang J, Yang Q, et al. Natural Sugar: A Green Assistance To Efficiently Exfoliate Inorganic Layered Nanomaterials. Inorg Chem 2018;57:5560-6.

[43] Pentecost A, Gour S, Mochalin V, Knoke I, Gogotsi Y. Deaggregation of nanodiamond powders using salt-and sugar-assisted milling. ACS Appl Mater Interfaces 2010;2:3289-94.

[44] Ge L, Zuo F, Liu J, Ma Q, Wang C, Sun D, et al. Synthesis and efficient visible light photocatalytic hydrogen evolution of polymeric g-C_3N_4 coupled with CdS quantum dots. J Phys Chem C 2012;116:13708-14.

[45] Wang Y, Hong J, Zhang W, Xu R. Carbon nitride nanosheets for photocatalytic hydrogen evolution: remarkably enhanced activity by dye sensitization. Catal Sci Technol 2013;3:1703-11.

[46] Jorge AB, Martin DJ, Dhanoa MT, Rahman AS, Makwana N, Tang J, et al. H_2 and O_2

evolution from water half-splitting reactions by graphitic carbon nitride materials. J Phys Chem C 2013;117:7178-85.

[47] Long B, Lin J, Wang X. Thermally-induced desulfurization and conversion of guanidine thiocyanate into graphitic carbon nitride catalysts for hydrogen photosynthesis. J Mater Chem A 2014;2:2942-51.

[48] Dong F, Wu L, Sun Y, Fu M, Wu Z, Lee S. Efficient synthesis of polymeric g-C_3N_4 layered materials as novel efficient visible light driven photocatalysts. J Mater Chem 2011;21:15171-4.

[49] Dong F, Sun Y, Wu L, Fu M, Wu Z. Facile transformation of low cost thiourea into nitrogen-rich graphitic carbon nitride nanocatalyst with high visible light photocatalytic performance. Catal Sci Technol 2012;2:1332-5.

[50] Dong F, Wang Z, Sun Y, Ho W-K, Zhang H. Engineering the nanoarchitecture and texture of polymeric carbon nitride semiconductor for enhanced visible light photocatalytic activity. J Colloid Interface Sci 2013;401:70-9.

[51] Zhang G, Zhang M, Ye X, Qiu X, Lin S, Wang X. Iodine modified carbon nitride semiconductors as visible light photocatalysts for hydrogen evolution. Adv Mater 2014;26:805-9.

[52] Martin DJ, Qiu K, Shevlin SA, Handoko AD, Chen X, Guo Z, et al. Highly efficient photocatalytic H_2 evolution from water using visible light and structure-controlled graphitic carbon nitride. Angew Chem Int Ed 2014;53:9240-5.

[53] Ma TY, Tang Y, Dai S, Qiao SZ. Proton-Functionalized Two-Dimensional Graphitic

Carbon Nitride Nanosheet: An Excellent Metal-/Label-Free Biosensing Platform. Small. 2014;10:2382-9.

[54] Yuan J, Wen J, Zhong Y, Li X, Fang Y, Zhang S, et al. Enhanced photocatalytic H_2 evolution over noble-metal-free NiS cocatalyst modified CdS nanorods/g-C3N4 heterojunctions. J Mater Chem A 2015;3:18244-55.

[55] Kruk M, Jaroniec M. Gas adsorption characterization of ordered organic-inorganic nanocomposite materials. Chem Mater 2001;13:3169-83.

[56] Li Y, Jin R, Xing Y, Li J, Song S, Liu X, et al. Macroscopic Foam-Like Holey Ultrathin g-C_3N_4 Nanosheets for Drastic Improvement of Visible-Light Photocatalytic Activity. Adv Energy Mater 2016;6:1601273.

[57] Yang P, Ou H, Fang Y, Wang X. A facile steam reforming strategy to delaminate layered carbon nitride semiconductors for photoredox catalysis. Angew Chem Int Ed 2017;56:3992-6.

[58] Zhang J, Zhang M, Sun RQ, Wang X. A facile band alignment of polymeric carbon nitride semiconductors to construct isotype heterojunctions. Angew Chem Int Ed 2012;51:10145-9.

[59] Fang J, Fan H, Li M, Long C. Nitrogen self-doped graphitic carbon nitride as efficient visible light photocatalyst for hydrogen evolution. J Mater Chem A 2015;3:13819-26.

[60] Iqbal W, Qiu B, Lei J, Wang L, Zhang J, Anpo M. One-step large-scale highly active g-C_3N_4 nanosheets for efficient sunlight-driven photocatalytic hydrogen production. Dalton Trans 2017;46:10678-84.

[61] Jeon IY, Zhang S, Zhang L, Choi HJ, Seo JM, Xia Z, et al. Edge-selectively sulfurized

graphene nanoplatelets as efficient metal-free electrocatalysts for oxygen reduction reaction: the electron spin effect. Adv Mater 2013;25:6138-45.

[62] Kudo A, Miseki Y. Heterogeneous photocatalyst materials for water splitting. Chem Soc Rev 2009;38:253-78.

[63] Shu J, Wang Z, Xia G, Zheng Y, Yang L, Zhang W. One-pot synthesis of AgCl@Ag hybrid photocatalyst with high photocatalytic activity and photostability under visible light and sunlight irradiation. Chem Eng J 2014;252:374-81.

[64] Huang N, Shu J, Wang Z, Chen M, Ren C, Zhang W. One-step pyrolytic synthesis of ZnO nanorods with enhanced photocatalytic activity and high photostability under visible light and UV light irradiation. J Alloys Compd 2015;648:919-29.

[65] Wen J, Xie J, Chen X, Li X. A review on g-C_3N_4-based photocatalysts. Appl Surf Sci 2017;391:72-123..